Exploring structural and electronic properties of topological insulator/graphene nano-heterostructures

Valentina Gallardo [a], Bárbara Arce [a], Francisco Muñoz [b], Rodolfo San Martín [a],
Irina Zubritskaya [c], Paula Giraldo-Gallo [d], Caleb Z. Zerger [c], Hari C. Manoharan [c],
Carolina Parra [e,f,*]

[a] *Departamento de Física, Universidad Técnica Federico Santa María, Avenida España 1680, Valparaíso, Chile*
[b] *Departamento de Física, Facultad de Ciencias, Universidad de Chile, 9170124 Santiago, Chile*
[c] *Department of Physics, Stanford University, Stanford, CA 94305, United States*
[d] *Department of Physics, Universidad de Los Andes, Bogotá 111711, Colombia*
[e] *Departamento de Ingeniería Mecánica, Universidad Técnica Federico Santa María, Avenida España 1680, Valparaíso, Chile*
[f] *Centro Científico Tecnológico de Valparaíso CCTVaL Universidad Técnica Federico Santa María, Valparaíso 2390123, Chile*

ABSTRACT

There is great interest in the study of topological insulator-based heterostructures due to expected emerging phenomena. However, a challenge of topological insulator (TI) research is the contribution of bulk conduction to the TI surface states. Both strain engineering and thickness control routes, which have been proposed to compensate for bulk doping, can be accessed through the use of nano-heterostructures consisting of topological insulator nanostructures grown on 2D materials. In this work, we report the synthesis of TI/graphene nano-heterostructures based on Bi_2Te_3 and Sb_2Te_3 nanoplatelets (NPs) grown on single-layer graphene. Various techniques were used to characterize this system in terms of morphology, thickness, composition, and crystal quality. We found that most of the obtained NPs are mainly <30 nm thick with thickness-dependent crystal quality, observed by Raman measurements. Thinner NPs (1 or 2 quintuple layers) tend to replicate the topography of the underlying single-layer graphene, according to roughness analysis. Finally, we show preliminary studies of their band structure obtained by Low Temperature Scanning Tunneling Microscopy, Scanning Tunneling Spectroscopy, and by Density Functional Theory. We observe a highly negative E_D value which can be attributed to the presence of defects.

Introduction

Topological insulators (TIs) are a new class of quantum material with a bulk gap and topologically protected massless Dirac surface states [1]. Since their prediction [2] and experimental realization [3], TIs have attracted great interest due to their potential for future applications in novel technologies such as spintronics [4], quantum computing [5], and low-dissipation electronic devices [6] as well as their potential to investigate fundamental phenomena such as Majorana fermions [7], proximity-induced superconductivity [8], and quantum anomalous Hall effect [9].

To exploit these unprecedented properties and phenomena, access to topological surface states is required. However, one of the most important challenges to overcome in the field of TI research is the presence of natural defects in the material, which produce intrinsic doping that leads to a contribution of the bulk states to the material's conductivity. Various routes have been used to diminish the bulk

conductance, for example, external doping [10–12] has been extensively used to compensate for bulk doping through a high residual dopant concentration but can lead to degrading electron carrier mobility [5]. The use of gating [13,14], different substrates [15,16], strain engineering [17–19], and thickness control [20] have also been proposed to manipulate the electronic structure of the material.

Among these methods, both strain engineering and thickness control are possible to obtain through the use of nano-heterostructures consisting of topological insulator nanostructures grown on 2D materials. The use of nanostructured TI has been proposed as an alternative to suppress bulk conductivity, due to their large surface-to-bulk ratio [21,22] and the possibility of controlling the topological surface state via the quantum confinement effect in the <30 nm thickness range [23,24]. Moreover, these nanostructures can be grown onto a variety of other materials, thus creating strained TI systems. The introduction of strain in TIs has been reported to tune the Dirac surface states [25] and to induce superconductivity [26] and van Hove singularities [27].

In addition, new emerging phenomena have been observed in various TI heterostructures systems such as induced magnetoresistance [28] and multiferroic properties [29] in Sb_2Te_3/GeTe heterostructures and an enhancement of optical sensitivity in TI/Ferromagnet heterostructures [30]. In the case of TI/graphene heterostructures, different proximity effects have been reported such as Rashba splitting and Dirac point (E_D) shift in the TI [31], the appearance of heavy Dirac fermions [32] and plasmonic excitations [33] across the heterojunction, and giant spin–orbit coupling in graphene, resulting in a new 2D system with non-trivial spin texture and high electron mobility [34–36].

To this day, the majority of studies on TI/graphene heterostructures have been made on thin films grown by MBE [15,37]. This method of synthesis, while useful to obtain high-quality crystals, is expensive, delicate, and slow, which makes it less accessible and has a lower production yield. Other methods to obtain these crystals include (i) mechanical exfoliation, which lacks control of the crystals' size and thickness, and (ii) solvothermal synthesis, which is a low-cost alternative, but the purity of the materials is not comparable to other techniques [38]. In contrast, chemical vapor deposition (CVD) appears as a powerful and low-cost bottom-up synthesis method that allows the achievement of high-quality TI nanostructures in a variety of substrates compatible with device applications [5]. Commonly used insulating flat substrates like SiO_2 or mica, don't interact with the electronic states of TIs. While this is useful for exploring TIs properties, the use of another quantum material, such as graphene, allows the study of proximity-induced emergent properties in the components of this heterostructure [39]. In this work, we focus on the growth and characterization of Bi_2Te_3 and Sb_2Te_3 nanostructures grown by CVD on single-layer graphene (SLG) to form nano-heterostructures. TIs synthesis parameters are tuned to keep TI nanostructures thickness mainly below the range (<30 nm) where the proximity and confinement effects have been reported [23,24].

Bi_2Te_3 and Sb_2Te_3 are chalcogenide materials that have a rhombohedral crystalline structure with a lattice constant of 0.4395 nm and 0.4262 nm respectively. Their structure (Fig. 1c) consists of five atomic sheets, called quintuple layers (QLs), with a thickness of 1 nm that are weakly bonded to each other by van der Waals (vdW) interactions. On the other side, graphene is a single layer of carbon atoms, arranged in a hexagonal lattice with a lattice constant of 0.246 nm. These materials bond to each other via interlayer vdW interactions, thus adding strain to the layers due to the initial lattice mismatch of the materials [19]. In the system presented here, Bi_2Te_3 and Sb_2Te_3 nanostructures can be epitaxially grown on graphene due to their small lattice mismatch of 2.7 % for Bi_2Te_3 [40] and 4 % for Sb_2Te_3 [41] thus resulting in a small in-plane strain.

In general, the electronic structure of TIs has been mostly determined by angle-resolved photoemission spectroscopy (ARPES) performed on MBE-grown thin films [42] or ultra-high vacuum (UHV) cleaved crystals [43]. Since ARPES signal cannot obtain local measurements due to beam size limitations, this restricts the access to high spatial resolution of TI band structure. In contrast, scanning tunneling spectroscopy (STS) allows access to local phenomena and has been used in the past to observe the absence of backscattering from nonmagnetic impurities of TI surface states [44,45]. However, few measurements of the local density of states (LDOS) of TI nanostructures have been carried out using STS, once again being focused on thin films [15] or UHV-cleaved crystals [45].

Considering this, we explore the structural and electronic properties of TI/SLG nano-heterostructures based on thin Bi_2Te_3 and Sb_2Te_3 nanoplatelets (NPs), grown on single-layer graphene. Synthesis parameters were tuned during growth to obtain TI nanostructures of <30 nm thicknesses to favor the appearance of surface states and interaction with SLG substrate. Various techniques were used to characterize these nano-heterostructures in terms of morphology, thickness, composition, and crystal quality, such as Raman Spectroscopy, Scanning Electron Microscopy (SEM), Energy-dispersive X-ray spectroscopy (EDS), Atomic Force Microscopy (AFM) and Low Temperature Scanning Tunneling Microscopy (LT-STM), together with preliminary theoretical and experimental studies of their band structure, obtained by Density Functional Theory (DFT) and STS.
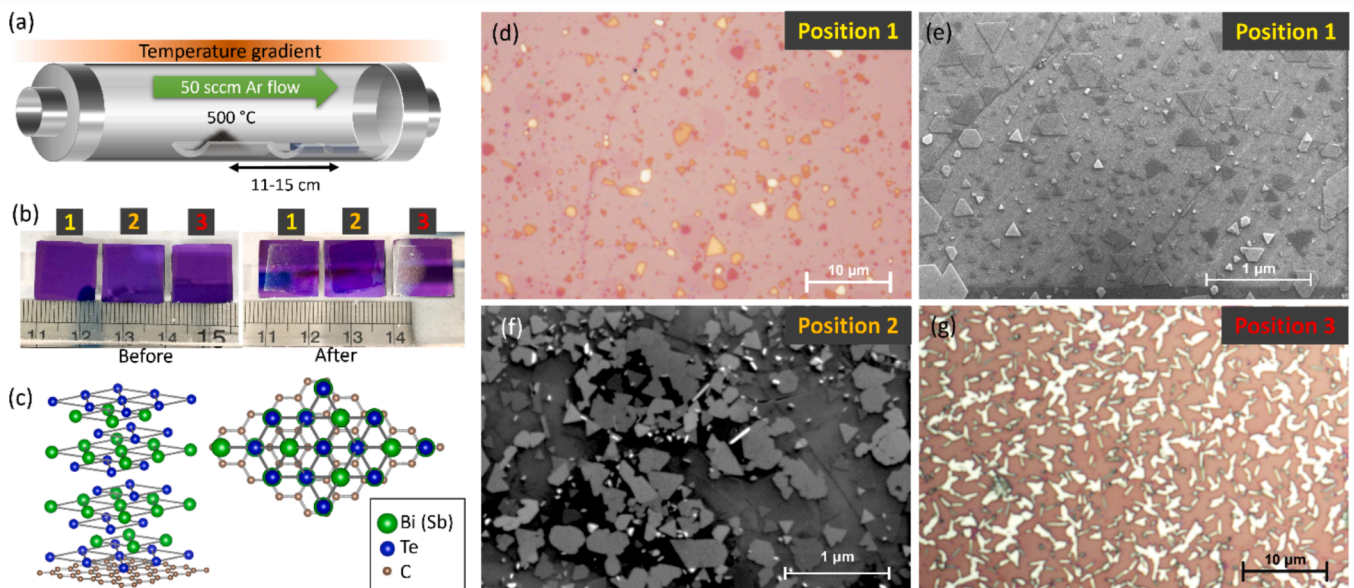
Fig. 1. **(a)** Schematic drawing of vapor–solid CVD deposition method. The precursor powder (either Bi_2Te_3 or Sb_2Te_3) is placed on the hot center of the tube furnace and the SLG/SiO_2 substrates are placed between 11–15 cm from the powder. **(b)** Substrates before synthesis of Bi_2Te_3/SLG nano-heterostructure and after synthesis of Bi_2Te_3/SLG nano-heterostructure. The ruler shows that the substrate in position 1 is placed between 11–12.5 cm away from the powder, the one in position 2 is between 12.5–14 cm and the one in position 3 is between 14–15.5 cm. See Fig. S2 for more details. **(c)** Crystal structure of Bi_2Te_3/SLG (Sb_2Te_3/SLG) nano-heterostructure. **(d)** Optical microscopy and **(e)** SEM image corresponding to the substrate in position 1 shown in **(b)**. **(f)** SEM image corresponding to the substrate in position 2 shown in **(b)**. **(g)** Optical microscopy image corresponding to the substrate in position 3 shown in **(b)**. See Fig. S4 for optical microscopy images of Sb_2Te_3/SLG samples.

Materials and methods

Before TI NP synthesis, single-layer graphene is transferred onto SiO$_2$ substrates (Silicon Prime Wafer, Oxide Thickness: 285 nm, N-doped) by a PMMA-assisted method [46]. Bi$_2$Te$_3$ and Sb$_2$Te$_3$ NPs were synthesized by a catalyst-free vapor transport and deposition process, which is described in Fig. 1a. The precursor powders for the growth of Bi$_2$Te$_3$/SLG (Bismuth(III) telluride, vacuum deposition grade, 99.999 %, metals basis – Alfa Aesar) or Sb$_2$Te$_3$/SLG (Antimony (III) telluride, 99.999 %, metals basis – Alfa Aesar) samples are placed on a quartz plate in the middle of one zone of the two-zone furnace (TFM2-1200 Across International). The SLG/SiO$_2$ substrates are placed 11–15 cm downstream of the powder source. Variations of other synthesis parameters were optimized before (See Fig. S1).

Synthesis is carried out for 5 min at a temperature of 500 °C and with an Ar flow of 50 sccm. Once the growth is complete, it is allowed to cool naturally (~3.5 °C/min), maintaining the flow of Ar and the system pressure (~0.3 torr). The TI NPs/SLG samples obtained were characterized by optical microscopy, SEM, and AFM to confirm the expected morphology and structure, together with Raman and EDS spectroscopy to obtain information on the crystalline quality and its composition. Finally, nano-heterostructures were characterized by LT-STM (STS) to obtain information on their local electronic properties, which were compared to DFT calculations.

Results

Regarding the effect of the growth parameters on the resulting NPs grown on SLG, it was observed that changes in the temperature of the substrate, the synthesis time, and the Ar gas flow affected the morphology and density of the grown nanostructures (Fig. 1d–g). These preliminary syntheses allowed us to obtain the growth parameters required for the target NP thickness.

As shown in Fig. 1b, three distinct positions for the different substrate temperatures (T$_S$) were identified, starting with position 1 at the highest T$_S$ and position 3 at the lowest T$_S$. After the growth process, differences between samples are evident to the naked eye (Fig. 1b). Optical microscopy and SEM images (Fig. 1d–g) show the difference between the nanostructures obtained at the different T$_S$ positions. Samples at position 1 (Fig. 1d and e) show the targeted nano-heterostructure of NPs that have a hexagonal or triangular shape, characteristic of the crystalline orientation of this material. These NPs have lateral dimensions between 0.1–2 μm, with a high growth density without percolation.

For the other two positions, located only 1–2 cm away from the sample at position 1 (Fig. 1f and g) NPs with Te rods (position 2) or only Te rods (position 3) were obtained, as confirmed with Raman spectroscopy (Fig. S3) that do not evidence the expected peaks of bismuth telluride and instead presented the peaks for crystalline tellurium [47,48]. These differences are also observed in Sb$_2$Te$_3$/SLG nano-heterostructures (Fig. S4). This small distance range in which ideal samples are synthesized demonstrates the importance of correctly tuning the studied growth parameters to minimize the waste of resources.

To study the composition of the NPs obtained, EDS and Raman spectroscopy measurements were performed. Fig. 2a shows an SEM image with EDS maps of Bi and Te signals overlapped and each element separately, confirming the homogeneity in the composition of the nanostructures. Fig. 2b shows the Raman spectra of three NPs of different thicknesses, starting from the thinnest (purple) to the thickest (yellow), these relative thicknesses being estimated according to the coloration of the NPs [49].

In the Raman spectra, the E$_g^2$ (~104 cm^{-1}) and A$_{1g}^2$ (~137 cm^{-1}) peaks characteristic of the bulk material [50] are marked. An increase in the FWHM is observed, when decreasing the thickness of the NPs, suggesting the presence of defects or impurities in the thinner NPs (See Table S1). Also, in the thinnest NP, the appearance of the A$_u^1$ peak (~119
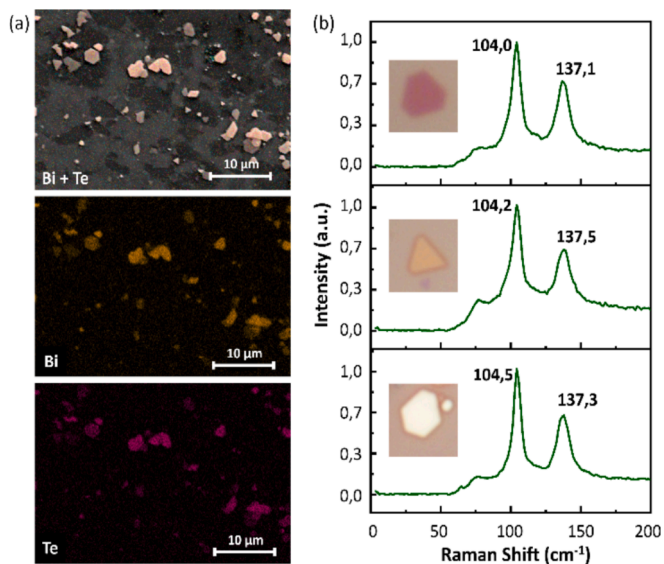

Fig. 2. (a) EDS maps of Bi$_2$Te$_3$/SLG nano-heterostructure, where the upper image shows a SEM image with both elements' signals combined, these signals are shown in the images below. **(b)** Raman spectra of individual Bi$_2$Te$_3$ NPs of different thicknesses, where the upper one is the thinnest and the bottom one is the thickest.

cm^{-1}) is observed, which has been reported in thin sheets and attributed to a break in the symmetry of the crystal in the third dimension due to the limited thickness [51]. Regarding the center of the peaks, a small variation (~0.5 cm^{-1}) is observed between the thickest and thinnest NPs, indicating little to no strain caused by the substrate in which it has been synthesized [52].

Height profile analysis of AFM images, as seen in Fig. 3a, shows that most of the NPs in the Bi$_2$Te$_3$/SLG nano-heterostructure were within the target thickness (<30 nm).

In addition, the NPs edge direction (with green arrows), suggests a preferential epitaxial growth for this heterostructured system. AFM measurements for the Sb$_2$Te$_3$/SLG nano-heterostructure show similar results (Fig. 3b).

Fig. 3a and b show NPs of different heights and wrinkles in graphene (see Fig. S5 for close-ups of these NPs and graphene wrinkles with their corresponding height profiles). Such wrinkles in graphene, intrinsic to the graphene transfer process, seem to perform as a barrier that stops the epitaxial growth of NPs, as evidenced by various NPs that present a truncated flat side where the NP meets the wrinkle, thus showing the importance of a flat substrate to favor in-plane lateral growth over out-of-plane vertical growth, and thus, to obtain thin NPs. See Fig. S6 for more details.

Surface height variations as a function of NP thickness are displayed in Fig. 3c. This plot shows the dispersion (FWHM) and the mean value for the NP and graphene surface height (blue for Bi$_2$Te$_3$, green for Sb$_2$Te$_3$, and red for graphene). From this data, no clear trend between the thickness of the NPs and their height mean value was obtained, however, an increase in the height dispersion was observed for the thinnest NPs.

This increase in height inhomogeneity for thinner NPs can be explained by the topographic characteristics of the underlying graphene affecting the growth of the NPs. Presumably, the graphene height inhomogeneity replicates on the surface of the NPs, whereas thicker NPs are less affected by the substrate and thus their height inhomogeneity homogenizes and tends to a bulk value. It is observed that thinner NPs present a height inhomogeneity similar to the one obtained for graphene and that the dispersion of the data decreases as the thickness of the NPs increases, which supports this interpretation. It was also observed that the root mean square (RMS) values follow a similar pattern for the
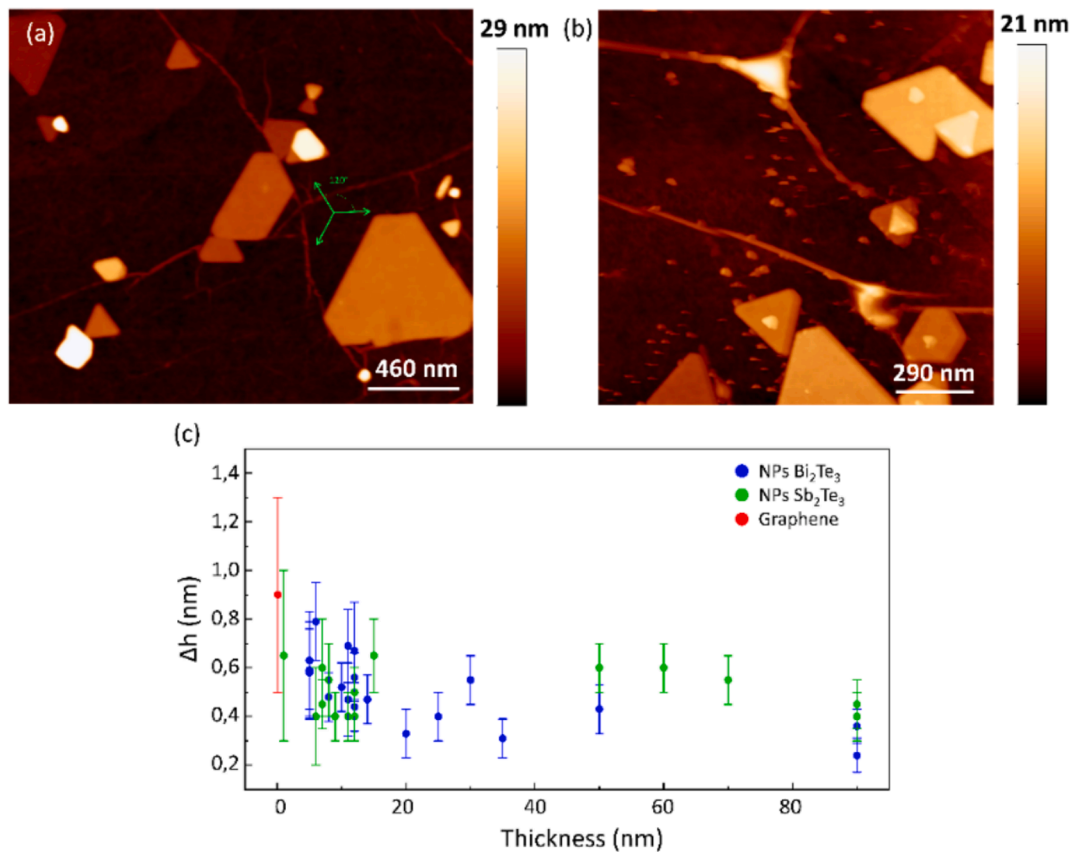
Fig. 3. (a) AFM image of Bi_2Te_3/SLG nano-heterostructure. The green arrows show the preferred in-plane epitaxial orientation of van der Waals epitaxy. **(b)** AFM image of Sb_2Te_3/SLG nano-heterostructure. **(c)** Height variation at the surface of NPs as a function of thickness. Graphene height variations are plotted for reference. Various NPs and different regions of graphene were used. Error bars represent the confidence interval in height graphs. Fig. S7 shows the roughness information of the systems. (For interpretation of the references to colour in this figure legend, the reader is referred to the web version of this article.)

Bi_2Te_3 NPs, however, the Sb_2Te_3 NPs don't show a clear tendency (Fig. S7).

Atomic-resolved topographic images of SLG were obtained using STM, as shown in Fig. 4a. Fig. 4b shows a zoom where the characteristic honeycomb hexagonal lattice can be seen. In Fig. 4c the corresponding fast Fourier transform (FFT) is observed, with which a lattice parameter of 1.41 ± 0.07 Å was obtained, an expected value for single-layer graphene. STM images show NPs as thin as 2 QL, like the one shown in Fig. 4d. Atomic resolved images of the NP (Fig. 4e) and FFT analysis

(Fig. 4f), confirm a lattice parameter of 4.52 ± 0.15 Å, consistent with Bi_2Te_3 structure.

Regarding their band structure, different studies have shown that these materials present band structures affected by their bulk states. In the case of Bi_2Te_3, the Dirac point is buried in the bulk valence band (BVB) while the Fermi level (E_F) is in the bulk conduction band (BCB), resulting in a n-doped material [53,54], whereas in the case of Sb_2Te_3, the Dirac point is located in the bulk band gap while the E_F is in the BVB, resulting in a p-doped material [15,54]. STS measurements on Bi_2Te_3
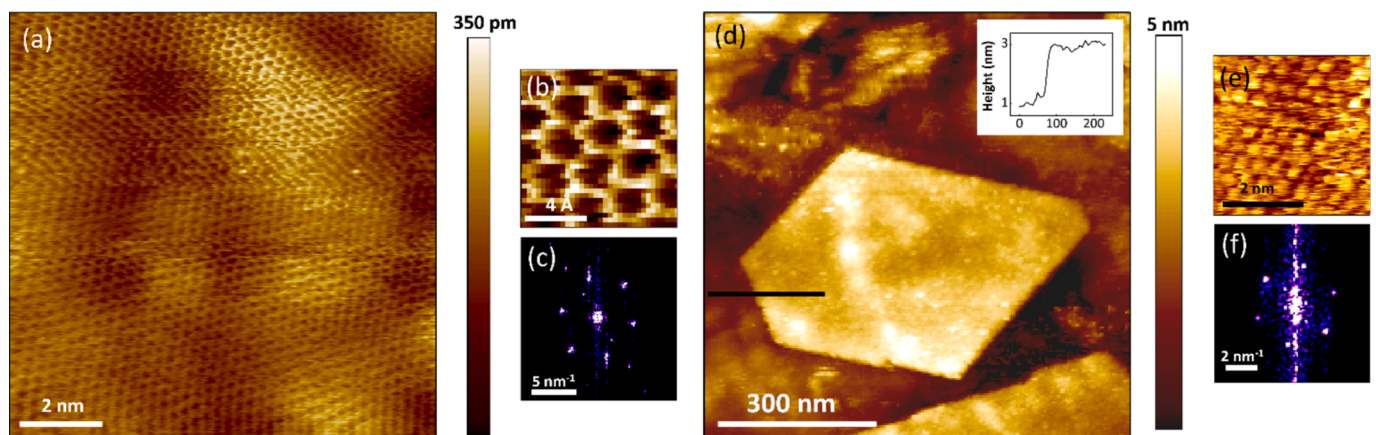
Fig. 4. (a) STM image of single-layer graphene transferred on SiO_2 with (b) close-up showing its characteristic honeycomb hexagonal lattice and (c) corresponding FFT. I = 30 pA; V_B = 0,8 V (d) STM image of 2 QL (height profile in inset) Bi_2Te_3 NP with (e) close-up showing its lattice and (f) corresponding FFT. I = 10 pA; V_B = 0,5 V, T = 70 K.

and Sb_2Te_3 nano-heterostructures show negative E_D values for both materials. Fig. 5a shows representative dI/dV spectra with a spatial resolution of 0.16 nm. These spectra are taken along a line in a 10 QL Bi_2Te_3 NP where a yellow dotted arrow marks the position of the average Dirac point (Fig. S8a and b). The Dirac points with respect to the Fermi level obtained by each spectrum can be seen in Fig. 5b, where the average value is marked with a dotted line. Fig. 5c and d show the same analysis for a 5 QL Sb_2Te_3 NP.

The Dirac point of Bi_2Te_3 NPs is obtained by finding the intersection between the linear surface states, marked with a yellow arrow in Fig. 5a, and the zero conduction line [15] (See Fig. S8c for the schematic of the surface band structure and dI/dV spectrum of Bi_2Te_3). A mean E_D value ~1.1 V below the Fermi level is found. This negative value for E_D is an expected result due to the effect of the intrinsic defects in this material [53]. It is known that Te-on-Bi antisite defects (Te_{Bi}) lower the position of the E_D in Bi_2Te_3 [53], thus, this kind of defect could contribute to the highly negative position of the E_D of the nano-heterostructure. Consistently, previous studies reported negative E_D values (but less negative) for Bi_2Te_3 single crystal (-0.35 V) [54] and a 10 QL Bi_2Te_3 NP grown on HOPG (-0.25 V) [20]. We performed DFT calculations for a 10 QL NP grown on SLG (See Fig. S9) to explore the observed behavior and a large difference in the location of the Dirac point between the experimental and calculated values. Once again, this

difference could be attributed to the intrinsic defects obtained during synthesis, as these defects are not present in our DFT calculations.

In addition, as seen in Fig. 5b, variations of the E_D were obtained, which suggest the presence of inhomogeneities in the composition of one individual NP that could be related to the presence of defects and impurities observed by Raman spectroscopy. Also, defects at the SiO_2 interface can result in a local shift of the Fermi level, given that the NP is just a few nm thick. In either case, point defects will create a local gradient in the potential energy, locally shifting the Fermi level and, hence, the position of the Dirac cone with respect to this level (a deeper discussion about possible defects is given in the Supplementary Material when discussing DFT calculations).

For Sb_2Te_3 NPs (Fig. 5c), the dI/dV spectra show a mean bulk band gap value of 0.26 V which is consistent with the reported 0.3–0.9 V gap value for Sb_2Te_3 *thin films* grown on graphene by MBE [15] but bigger than our 0.1 V value calculated by DFT (Fig. S10). This could be explained by an incorrect prediction of the band gap of the material and/ or the presence of defects. For this material, the Dirac point lies within this gap, so our observed bulk band gap being between -0.05 V to -0.35 V suggests a negative E_D value due to the position of the bulk band gap to the Fermi level. It is known that this material has intrinsic positive doping, however, as mentioned before, a shift in the E_D towards negative values as the thickness of NPs decreases has been observed on
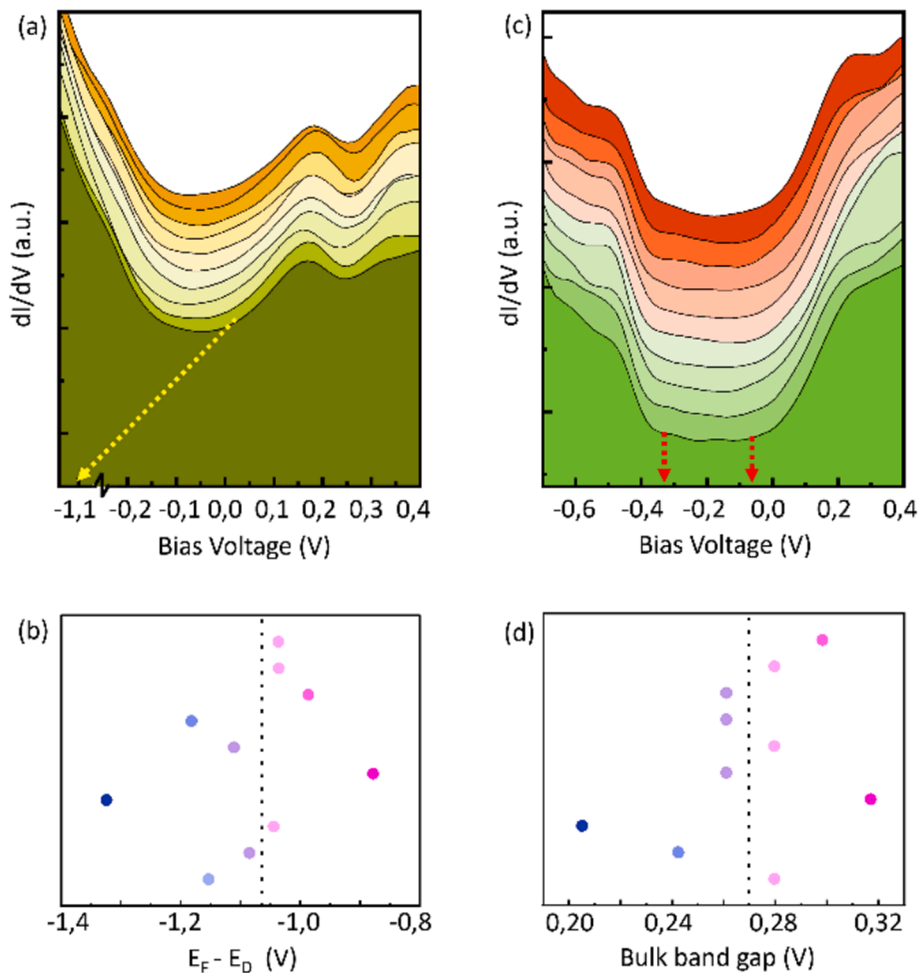
Fig. 5. (a) Measurements of dI/dV along a line in a Bi_2Te_3 NP of 10 QL. The yellow dotted arrow shows the E_D mean value. For clarity purposes, an arbitrary offset was added to every dI/dV spectrum. (b) Position of the Dirac point with respect to the Fermi level for each spectrum displayed in (a) with the mean value marked with a black dotted line. Pink dots are values over the mean E_D and purple dots are values below. (c) Measurements of dI/dV along a line in a Sb_2Te_3 NP of 5 QL. The red dotted arrows show the mean bulk band gap value. For clarity, an arbitrary offset was added to every dI/dV spectra. (d) The bulk band gap for each spectrum is displayed in (c) with the mean value marked with a black dotted line. Pink dots are values over the mean bulk band gap and purple dots are values below. See complementary information in Fig. S8. (For interpretation of the references to colour in this figure legend, the reader is referred to the web version of this article.)

Sb_2Te_3 *thin films* [15]. Since the Sb_2Te_3 NP presented here is only 5 QL thick, this negative value is consistent with these previous reports.

Conclusions

We explore the properties of TI/SLG nano-heterostructures based on <30 nm thick Bi_2Te_3 and Sb_2Te_3 NPs, grown on monolayer graphene by CVD. The influence of SLG substrate on the topography and growth mode of grown TI NPs was studied. Crystalline quality decreases with NP thickness and the appearance of peaks linked to a break in the symmetry of the system due to size limitations is observed, while the thicker NPs showed the expected bulk spectra.

The STS measurements showed highly negative values for the E_D for both nano-heterostructures. This is probably connected to the presence of defects in the composition of the NPs, such as Te_{Bi} defects, that can shift the Fermi energy up. Since a diminution of crystal quality on thinner NPs was observed, this is a possible origin for this negative value of the E_D. The NPs also showed E_D spatial inhomogeneities within a single NP, which is also consistent with the presence of defects. DFT calculations confirmed the influence of the substrate in shifting the Dirac point in these systems.

Further STS studies on this nano-heterostructure system will provide insight into a possible NP thickness dependence of E_D.

Control of graphene morphology and the thickness of NPs in this kind of nano-heterostructure could open a new route to generate buckling in TI materials that will lead to emergent electronic properties, such as pseudo-magnetic fields reported on graphene-based strained structures.

CRediT authorship contribution statement

Valentina Gallardo: Writing – original draft, Software, Methodology, Investigation, Formal analysis. **Bárbara Arce:** Methodology, Investigation. **Francisco Muñoz:** Writing – review & editing, Software, Resources, Methodology, Funding acquisition. **Rodolfo San Martín:** Investigation. **Irina Zubritskaya:** Investigation. **Paula Giraldo-Gallo:** Writing – review & editing, Software, Resources, Funding acquisition. **Caleb Z. Zerger:** Investigation, Writing – review & editing. **Hari C. Manoharan:** Writing – review & editing, Resources, Funding acquisition. **Carolina Parra:** Writing – review & editing, Supervision, Resources, Project administration, Methodology, Investigation, Funding acquisition, Conceptualization.

Declaration of competing interest

The authors declare that they have no known competing financial interests or personal relationships that could have appeared to influence the work reported in this paper.

Appendix A. Supplementary data

Supplementary data to this article can be found online at https://doi.org/10.1016/j.rinp.2024.108058.

Data availability

The data that support the findings of this study are available from the corresponding author upon reasonable request.

References

[1] Kane CL, Mele EJ. Topological order and the quantum spin hall effect. Phys Rev Lett 2005;95:146802. https://doi.org/10.1103/PhysRevLett.95.146802.

[2] Bernevig BA, Hughes TL, Zhang S-C. Quantum spin hall effect and topological phase transition in HgTe quantum wells. Science 1979;2006(314):1757–61. https://doi.org/10.1126/science.1133734.

[3] König M, Wiedmann S, Brüne C, Roth A, Buhmann H, Molenkamp LW, et al. Quantum spin hall insulator state in HgTe quantum wells. Science 1979;2007 (318):766–70. https://doi.org/10.1126/science.1148047.

[4] Tokura Y, Yasuda K, Tsukazaki A. Magnetic topological insulators. Nat Rev Phys 2019;1:126–43. https://doi.org/10.1038/s42254-018-0011-5.

[5] Liu P, Williams JR, Cha JJ. Topological nanomaterials. Nat Rev Mater 2019;4: 479–96. https://doi.org/10.1038/s41578-019-0113-4.

[6] Nadeem M, Hamilton AR, Fuhrer MS, Wang X. Quantum anomalous hall effect in magnetic doped topological insulators and ferromagnetic spin-gapless semiconductors—a perspective review. Small 2020;16:1–13. https://doi.org/10.1002/smll.201904322.

[7] Hasan MZ, Kane CL. Colloquium: topological insulators. Rev Mod Phys 2010;82: 3045–67. https://doi.org/10.1103/RevModPhys.82.3045.

[8] He L, Kou X, Wang KL. Review of 3D topological insulator thin-film growth by molecular beam epitaxy and potential applications. Physica Status Solidi (RRL) – Rapid Res Lett 2013;7:50–63. https://doi.org/10.1002/pssr.201307003.

[9] He K, Wang Y, Xue Q-K. Topological materials: quantum anomalous hall system. Annu Rev Condens Matter Phys 2018;9:329–44. https://doi.org/10.1146/annurev-conmatphys-033117-054144.

[10] Li H, Song YR, Yao M-Y, Zhu F, Liu C, Gao CL, et al. Carrier density dependence of the magnetic properties in iron-doped Bi2Se3 topological insulator. J Appl Phys 2013;113. https://doi.org/10.1063/1.4788834.

[11] Ren Z, Taskin AA, Sasaki S, Segawa K, Ando Y. Fermi level tuning and a large activation gap achieved in the topological insulator Bi2Te2Se by Sn doping. Phys Rev B 2012;85:155301. https://doi.org/10.1103/PhysRevB.85.155301.

[12] Tanaka Y, Nakayama K, Souma S, Sato T, Xu N, Zhang P, et al. Evolution of electronic structure upon Cu doping in the topological insulator Bi2Se3. Phys Rev B 2012;85:125111. https://doi.org/10.1103/PhysRevB.85.125111.

[13] Xiu F, He L, Wang Y, Cheng L, Chang L-T, Lang M, et al. Manipulating surface states in topological insulator nanoribbons. Nat Nanotechnol 2011;6:216–21. https://doi.org/10.1038/nnano.2011.19.

[14] Yao J, Shao J, Wang Y, Zhao Z, Yang G. Ultra-broadband and high response of the Bi2Te3–Si heterojunction and its application as a photodetector at room temperature in harsh working environments. Nanoscale 2015;7:12535–41. https://doi.org/10.1039/C5NR02953H.

[15] Jiang Y, Sun YY, Chen M, Wang Y, Li Z, Song C, et al. Fermi-level tuning of epitaxial Sb2Te3 thin films on graphene by regulating intrinsic defects and substrate transfer doping. Phys Rev Lett 2012;108:066809. https://doi.org/10.1103/PhysRevLett.108.066809.

[16] Zalic A, Dvir T, Steinberg H. High-density carriers at a strongly coupled interface between graphene and a three-dimensional topological insulator. Phys Rev B 2017; 96:075104. https://doi.org/10.1103/PhysRevB.96.075104.

[17] Liu Y, Li YY, Rajput S, Gilks D, Lari L, Galindo PL, et al. Tuning Dirac states by strain in the topological insulator Bi2Se3. Nat Phys 2014;10:294–9. https://doi.org/10.1038/nphys2898.

[18] Schindler C, Wiegand B, Sichau J, Tiemann L, Nielsch K, Zierold R, et al. Strain-induced Dirac state shift in topological insulator Bi2Se3 nanowires. Appl Phys Lett 2017;111:171601. https://doi.org/10.1063/1.5001929.

[19] Vermeulen PA, Mulder J, Momand J, Kooi BJ. Strain engineering of van der Waals heterostructures. Nanoscale 2018;10:1474–80. https://doi.org/10.1039/C7NR07607J.

[20] Parra C, Rodrigues da Cunha TH, Contryman AW, Kong D, Montero-Silva F, Rezende Gonçalves PH, et al. Phase separation of dirac electrons in topological insulators at the spatial limit. Nano Lett 2017;17:97–103. https://doi.org/10.1021/acs.nanolett.6b03506.

[21] Kim YS, Brahlek M, Bansal N, Edrey E, Kapilevich GA, Iida K, et al. Thickness-dependent bulk properties and weak antilocalization effect in topological insulator Bi2Se3. Phys Rev B 2011;84:073109. https://doi.org/10.1103/PhysRevB.84.073109.

[22] Xia B, Ren P, Sulaev A, Liu P, Shen S-Q, Wang L. Indications of surface-dominated transport in single crystalline nanoflake devices of topological insulator Bi1.5Sb0.5Te1.8Se1.2. Phys Rev B 2013;87:085442. https://doi.org/10.1103/PhysRevB.87.085442.

[23] Hong SS, Kong D, Cui Y. Topological insulator nanostructures. MRS Bull 2014;39: 873–9. https://doi.org/10.1557/mrs.2014.196.

[24] Giraud R, Dufouleur J. Quantum transport in nanostructures of 3D topological insulators. Physica Status Solidi (b) 2021;258. https://doi.org/10.1002/pssb.202000066.

[25] Flötotto D, Bai Y, Chan Y-H, Chen P, Wang X, Rossi P, et al. In situ strain tuning of the dirac surface states in Bi2Se3 films. Nano Lett 2018;18:5628–32. https://doi.org/10.1021/acs.nanolett.8b02105.

[26] Charpentier S, Galletti L, Kunakova G, Arpaia R, Song Y, Baghdadi R, et al. Induced unconventional superconductivity on the surface states of Bi2Te3 topological insulator. Nat Commun 2017;8:2019. https://doi.org/10.1038/s41467-017-02069-z.

[27] Kim T-H, Jeong K, Park BC, Choi H, Park SH, Jung S, et al. Tuning the Fermi level with topological phase transition by internal strain in a topological insulator Bi2Se3 thin film. Nanoscale 2016;8:741–51. https://doi.org/10.1039/C5NR06086A.

[28] Tominaga J, Saito Y, Mitrofanov K, Inoue N, Fons P, Kolobov AV, et al. A magnetoresistance induced by a nonzero berry phase in GeTe/Sb2Te3 chalcogenide superlattices. Adv Funct Mater 2017:27. https://doi.org/10.1002/adfm.201702243.

[29] Tominaga J, Kolobov AV, Fons PJ, Wang X, Saito Y, Nakano T, et al. Giant multiferroic effects in topological GeTe-Sb2Te3 superlattices. Sci Technol Adv Mater 2015;16:014402. https://doi.org/10.1088/1468-6996/16/1/014402.

[30] Li X, Semenov YG, Kim KW. Thin-film topological insulator-ferromagnet heterostructures for terahertz detection. Appl Phys Lett 2014;104. https://doi.org/10.1063/1.4865423.

[31] Song H-D, Sheng D, Wang A-Q, Li J-G, Yu D-P, Liao Z-M. Topological transport in Dirac electronic systems: a concise review. Chin Phys B 2017;26:037301. https://doi.org/10.1088/1674-1056/26/3/037301.

[32] Cao W, Zhang R-X, Tang P, Yang G, Sofo J, Duan W, et al. Heavy Dirac fermions in a graphene/topological insulator hetero-junction. 2d Mater 2016;3:034006. https://doi.org/10.1088/2053-1583/3/3/034006.

[33] Liu Y, Wei T, Cui P, Li X, Zhang Z. Emergent plasmonic excitations in Mexican-hat and bell-shaped bands of hybridized Dirac electrons in graphene/topological insulator heterostructures. Phys Rev B 2022;105:195150. https://doi.org/10.1103/PhysRevB.105.195150.

[34] Zhang J, Triola C, Rossi E. Proximity effect in graphene–topological-insulator heterostructures. Phys Rev Lett 2014;112:096802. https://doi.org/10.1103/PhysRevLett.112.096802.

[35] Jin K-H, Jhi S-H. Proximity-induced giant spin-orbit interaction in epitaxial graphene on a topological insulator. Phys Rev B 2013;87:075442. https://doi.org/10.1103/PhysRevB.87.075442.

[36] Zollner K, Fabian J. Heterostructures of graphene and topological insulators Bi2Se3, Bi2Te3, and Sb2Te3. Physica Status Solidi (b) 2021;258. https://doi.org/10.1002/pssb.202000081.

[37] Yin Y, Wang G, Liu C, Huang H, Chen J, Liu J, et al. Moiré-pattern-modulated electronic structures in Sb2Te3/graphene heterostructure. Nano Res 2022;15:1115–9. https://doi.org/10.1007/s12274-021-3613-7.

[38] Tian W, Yu W, Shi J, Wang Y. The property, preparation and application of topological insulators: a review. Materials 2017;10:814. https://doi.org/10.3390/ma10070814.

[39] Žutić I, Matos-Abiague A, Scharf B, Dery H, Belashchenko K. Proximitized materials. Mater Today 2019;22:85–107. https://doi.org/10.1016/j.mattod.2018.05.003.

[40] Qiao H, Yuan J, Xu Z, Chen C, Lin S, Wang Y, et al. Broadband photodetectors based on graphene–Bi2Te3 heterostructure. ACS Nano 2015;9:1886–94. https://doi.org/10.1021/nn506920z.

[41] Singh S, Kim S, Jeon W, Dhakal KP, Kim J, Baik S. Graphene grain size-dependent synthesis of single-crystalline Sb2Te3 nanoplates and the interfacial thermal transport analysis by Raman thermometry. Carbon N Y 2019;153:164–72. https://doi.org/10.1016/j.carbon.2019.07.017.

[42] Zhang K, Pan H, Wei Z, Zhang M, Song F, Wang X, et al. Synthesis and magnetotransport properties of Bi2Se3 nanowires. Chin Phys B 2017;26:096101. https://doi.org/10.1088/1674-1056/26/9/096101.

[43] Kong D, Dang W, Cha JJ, Li H, Meister S, Peng H, et al. Few-layer nanoplates of Bi2Se3 and Bi2Te3 with highly tunable chemical potential. Nano Lett 2010;10:2245–50. https://doi.org/10.1021/nl101260j.

[44] Ngabonziza P, Stehno MP, Koster G, Brinkman A. In situ characterization tools for Bi2Te3 topological insulator nanomaterials. In: In-situ characterization techniques for nanomaterials, Berlin, Heidelberg: Springer Berlin Heidelberg; 2018, p. 223–50. doi: 10.1007/978-3-662-56322-9_7.

[45] Alpichshev Z, Analytis JG, Chu J-H, Fisher IR, Chen YL, Shen ZX, et al. STM imaging of electronic waves on the surface of Bi2Te3: topologically protected surface states and hexagonal warping effects. Phys Rev Lett 2010;104:016401. https://doi.org/10.1103/PhysRevLett.104.016401.

[46] Parra C, Aristizabal J, Arce B, Montero-Silva F, Lascano S, Henriquez R, et al. Graphene coating as an effective barrier to prevent bacteria-mediated dissolution of gold. Metals (Basel) 2021;11:147. https://doi.org/10.3390/met11010147.

[47] Khatun S, Banerjee A, Pal AJ. Nonlayered tellurene as an elemental 2D topological insulator: experimental evidence from scanning tunneling spectroscopy. Nanoscale 2019;11:3591–8. https://doi.org/10.1039/C8NR09760G.

[48] Du Y, Qiu G, Wang Y, Si M, Xu X, Wu W, et al. One-dimensional van der Waals material tellurium: Raman spectroscopy under strain and magneto-transport. Nano Lett 2017;17:3965–73. https://doi.org/10.1021/acs.nanolett.7b01717.

[49] Yang F, Sendova M, Jacobs-Gedrim RB, Song ES, Green A, Thiesen P, et al. Rapid optical determination of topological insulator nanoplate thickness and oxidation. AIP Adv 2017;7. https://doi.org/10.1063/1.4973403.

[50] Shahil KMF, Hossain MZ, Teweldebrhan D, Balandin AA. Crystal symmetry breaking in few-quintuple Bi2Te3 films: applications in nanometrology of topological insulators. Appl Phys Lett 2010;96. https://doi.org/10.1063/1.3396190.

[51] Shahil KMF, Hossain MZ, Goyal V, Balandin AA. Micro-Raman spectroscopy of mechanically exfoliated few-quintuple layers of Bi2Te3, Bi2Se3, and Sb2Te3 materials. J Appl Phys 2012;111. https://doi.org/10.1063/1.3690913.

[52] Dang W, Peng H, Li H, Wang P, Liu Z. Epitaxial heterostructures of ultrathin topological insulator nanoplate and graphene. Nano Lett 2010;10:2870–6. https://doi.org/10.1021/nl100938e.

[53] Wang G, Zhu X, Sun Y, Li Y, Zhang T, Wen J, et al. Topological insulator thin films of Bi2Te3 with controlled electronic structure. Adv Mater 2011;23:2929–32. https://doi.org/10.1002/adma.201100678.

[54] Kong D, Chen Y, Cha JJ, Zhang Q, Analytis JG, Lai K, et al. Ambipolar field effect in the ternary topological insulator (BixSb1–x)2Te3 by composition tuning. Nat Nanotechnol 2011;6:705–9. https://doi.org/10.1038/nnano.2011.172.